Applied Physics Letters 116 (2020) 182103

Approaching the high intrinsic electrical resistivity of NbO_2 in epitaxially grown films

Julian Stoever[a,*], Jos E. Boschker[a], Saud Bin Anooz[a], Martin Schmidbauer[a], Peter Petrik[b], Jutta Schwarzkopf[a], Martin Albrecht[a], Klaus Irmscher[a]

[a] Leibniz-Institut für Kristallzüchtung, Max-Born-Str. 2, 12489 Berlin, Germany
[b] Institute for Technical Physics and Materials Science, Centre for Energy Research, Konkoly Thege Miklós Str 29-33, 1121 Budapest, Hungary
* Author to whom correspondence should be addressed: julian.stoever@ikz-berlin.de

Abstract

NbO_2 is a promising candidate for resistive switching devices due to an insulator-metal transition above room temperature, which is related to a phase transition from a distorted rutile structure to undistorted one. However, the electrical resistivity of the NbO_2 thin-films produced so far has been too low to achieve high on-off switching ratios. Here we report on the structural, electrical and optical characterization of single-crystalline NbO_2 (001) thin-films grown by pulsed laser deposition on MgF_2 (001) substrates. An annealing step reduced the full width at half maximum of the NbO_2 (004) X-ray Bragg reflection by one order of magnitude, while the electrical resistivity of the films increased by two orders of magnitude to about 1 kΩcm at room-temperature. Temperature dependent resistivity measurements of an annealed sample revealed that below 650 K two deep-level defects with activation energies of 0.25 eV and 0.37 eV dominate the conduction, while above 650 K intrinsic conduction prevails. Optical characterization by spectroscopic ellipsometry and by absorption measurements with the electric field vector of the incident light perpendicular to the *c*-axis of the distorted rutile structure indicates the onset of fundamental absorption at about 0.76 eV at room temperature, while at 4 K the onset shifts to 0.85 eV. These optical transitions are interpreted to take place across the theoretically predicted indirect band gap of distorted rutile NbO_2.

Mott-Peierls metal-insulator transitions (MIT), which were shown in several transition-metal oxides,[1,2] can be utilized in devices like optical switches[3], sensors[4], transistors or memory devices[1,5–7]. However, the phase-transition temperature, often below or close to room temperature, prevent the materials from being used in commercial applications. This has recently led to an increased interest in NbO_2 since its metal-insulator transition temperature is at around 830 °C.[8–10] The MIT comes along with a structural phase-transition from the low temperature, semiconducting distorted rutile structure to a metallic undistorted rutile structure.[8–10] A dimerization of the Nb-Nb d-orbitals along the [001]-direction in distorted rutile leads to the formation of a band gap.[11,12] In this direction, the strongest change in resistivity due to the metal-insulator transition can be observed , making this crystal orientation interesting for device applications.[5,13–15] For lateral resistive switching devices, NbO_2 layers with an in-plane [001] direction have been demonstrated.[14,16] However, low room-temperature resistivity values of only several Ωcm[17–20] have been reported for thin-films so far compared to the intrinsic resistivity value of 10 kΩcm measured for bulk crystals.[21,22] To improve the resistivity ratio at the MIT for thin-film devices, thus, higher room-temperature resistivity is desirable.[5] Besides the low resistivity, also a broad range of optical band gap values from 0.5 eV to 1.2 eV were reported, indicating that defects influence the properties of the thin-films.[10,14,23]

In this work, the growth of out-of-plane c-oriented NbO_2 thin-films will be shown, which may be used in vertical device structures having a higher integration density compared to lateral devices as well as enabling the usage in memristive crossbar arrays.[24] With the vertical structures, high electric field

strengths can be achieved, allowing easy switching between the states. It will be shown that a post-growth annealing step above the phase-transition temperature can increase the resistivity of NbO_2 thin-film layers up to 950 Ωcm. Temperature-dependent resistivity measurements are used to identify deep levels within the band gap of the semiconducting phase. Spectroscopic ellipsometry (SE) and absorption spectroscopy (AS) measurements are used to determine the optical band gap of NbO_2 (001) thin-films.

Rutile NbO_2(001) thin-films were grown on MgF_2(001) substrates by pulsed-laser deposition (PLD). The crystallographic orientation was determined by high-resolution x-ray diffraction. ω-2θ scans are shown together with the corresponding rocking curves in the Supplementary Material (Fig. S1). Below the phase-transition temperature, NbO_2 is in a tetragonal phase (space group $I4_1/a$)[25], whose *c*-axis differs from the rutile ($P4_2/mnm$)[26] *c*-axis. However, since the deviation of the atomic positions is small compared to the rutile structure,[27] also the low-temperature phase can be treated as a distorted, pseudo rutile structure. The substrate dimensions are 5x5x0.5 mm³, having a lapped back-side and a for epitaxy polished front-side. MgF_2 has a rutile structure with lattice parameters $a_{\mathrm{MgF_2}} = 4.628$ Å and $c_{\mathrm{MgF_2}} = 3.045$ Å,[28] compared to $a_{\mathrm{NbO_2}} = 4.8463$ Å and $c_{\mathrm{NbO_2}} = 3.0315$ Å,[26] resulting in an in-plane lattice mismatch of 4.5% according to $\left(a_{\mathrm{NbO_2}} - a_{\mathrm{MgF_2}}\right)/a_{\mathrm{NbO_2}}$. The films are plastically relaxed, which was confirmed by x-ray reciprocal space maps (see Supplementary Material Fig. S1). For the basic investigations by atomic force microscopy (AFM), high-resolution x-ray diffraction (HRXRD), and room-temperature resistivity measurements, NbO_2 thin-films with a thickness of 100 nm were used due to a shorter process time. For optical measurements as well as for the temperature-dependent resistivity measurements, a layer thickness of 1000 nm was chosen to increase measurement sensitivity and accuracy, respectively.

For PLD, a Nb_2O_5 target (99.9985% purity) was placed at a distance of 60 mm from the substrate. An aperture was used to cut off the flanks of the Gaussian laser beam of a KrF laser, resulting in laser energy of 65 mJ/pulse and a fluence of 2 J/cm². For the deposition, a repetition rate of 5 Hz was employed. A background pressure of 0.09 mbar consisting of 99.9% Ar and 0.1% O_2 was present during the whole process. Before the deposition, the substrates were degassed at 500 °C. During the deposition, the temperature was increased from initially 350 °C to the final growth temperatures of 500 °C to 700 °C, using a heating rate of 5-10 K/min. The average growth rate was (1.7 ± 0.5) nm/min. The samples were cooled down with a reduced background pressure of 10^{-6} mbar. In order to investigate the influence of a post-growth annealing step, samples grown with the recipe described above were annealed. Post-growth annealing was performed by increasing the sample temperature directly after growth to 880 °C, which is above the phase-transition temperature, and held them at that temperature for one hour. As-grown (without annealing) and post-growth annealed samples were then investigated for their structural and electrical properties to assess the influence of annealing on the NbO_2 thin-films.

A *Bruker Icon* atomic force microscope operated in *PeakForce Tapping*™ mode was used for surface morphology studies. The average grain size was determined by using the *Gwyddion* watershed masking and statistics tool.[29] The structural properties were studied by HRXRD with a *Bruker D8 Discover* using well collimated and monochromatic Cu $K\alpha_1$ radiation.

A *Woollam M-2000DI* rotating compensator ellipsometer with a spectral range of 0.73 – 6.48 eV was used to determine the complex dielectric function and the optical band gap within the isotropic NbO_2(001) plane. The complex reflectance ratio *R* of the light polarized parallel to the plane of incidence (r_p) and the perpendicularly polarized wave (r_s) is measured. It can be expressed by the amplitude ψ and the phase difference Δ with[30]

$$R = \frac{r_p}{r_s} = tan(\psi)\, e^{i\Delta}. \qquad (1)$$

A large angle of incidence of 70° was used for SE, providing an electric field primarily aligned in the (001) plane of the thin film, which is optically isotropic in the tetragonal crystal structure. The isotropy of the dielectric function was confirmed by rotating the sample around the [001] axis. For the evaluation of the SE data, a model consisting of a four-component stack composed of air/surface roughness/NbO_2 thin-film/MgF_2 substrate was used. The optical properties of the surface roughness layer are analyzed by a Bruggeman effective medium approximation[31] consisting of a 50% bulk film/ 50% void mixture. The amplitude ψ and phase difference Δ were fitted over the spectral range using optical dispersion models based on Gaussian type oscillators.

A double beam, double monochromator spectrophotometer (*PerkinElmer Lambda 1050*) was used for absorption measurements in the spectral range from 1600 nm to 930 nm. Low-temperature measurements between 4 K and 300 K were performed in a helium-flow cryostat (*Oxford Instruments OptistatCF*). Substrate backsides were polished to suppress surface scattering. A baseline correction was performed for 0% transmission (blocked beam) and 100% transmission. The 100% transmission correction was performed with a bare, back-side polished MgF_2 wafer in the sample beam to subtract the substrate absorption. The incident beam was along the [001] axis corresponding to a light polarization with the electric field vector perpendicular to [001], and thus again, the absorption coefficient was measured within the isotropic (001) plane. Using the transfer-matrix method,[32] the absorption coefficient for an air/thin-film/substrate stack can be calculated by using

$$\alpha = -\frac{1}{d} ln\left(\frac{\sqrt{(1-R_{01})^2(1-R_{12})^2+4T^2R_{01}R_{12}}-(1-R_{01})(1-R_{12})}{2TR_{01}R_{12}}\right), \qquad (2)$$

where T is the transmission measured in the experiment, and d is the thin-film thickness. The reflectivity R_{ij} at an interface of the layer stack can be calculated from the refractive indices n_i with $R_{ij} = \left(n_i - n_j\right)^2 / \left(n_i + n_j\right)^2$, where *i,j = 0,1,2* are the indices for air ($n_0 \approx 1$), the NbO_2 layer, and the MgF_2 substrate, respectively. The refractive indices n_1 and n_2 were measured by spectroscopic ellipsometry.

The electrical resistivity of the epitaxial layers was measured in Van-der-Pauw geometry over the temperature range from 165 K to 870 K. At the corners of the samples, ohmic contacts (50 nm titanium/50 nm gold) with a diameter of roughly 500 µm were deposited by electron beam evaporation through a shadow mask. For investigations below room temperature, a DC *LakeShore Hall System* was used. The sample was cooled in a closed-cycle helium refrigerator. For temperatures above room temperature, an AC *Fraunhofer Hall 1100K* setup was used. The sample was heated in a sealed gas chamber containing a nitrogen atmosphere with a base pressure of 700 mbar at room-temperature, which increased to 950 mbar at 870 K.

In order to investigate the influence of the post-growth annealing, the as-grown and annealed samples were characterized with respect to their structural and electrical properties. The surface morphologies investigated by AFM of the as-grown (Fig. 1(a)) and the annealed (Fig. 1(b)) samples indicate the presence of grains in both cases. While the as-grown film exhibits grain sizes in the sub-10 nm range, the annealed layer shows significantly larger grain sizes up to 60 nm. Besides, a tentative orientation of the grains along the NbO_2 [100] and [010] directions is observed for the annealed sample. The RHEED pattern (see Supplementary Fig. S2) shows a superposition of 3D contributions (spotty diffraction peaks) and 2D contributions (streaky diffraction peaks lying on a circle), as well as a single-domain in-plane orientation. This agrees well with the AFM images, where islands with flat surfaces are visible. Fig. 1(c) shows the azimuthal φ-scans around the asymmetric (222) Bragg reflection of NbO_2 for both samples. The sharp and strong peak located at $\varphi = 0°$ can be assigned to the single-crystalline MgF_2

substrate. The broad and weak feature in the vicinity of the substrate peak originates from the NbO_2 thin film. The as-grown sample shows a broad intensity profile indicating high mosaicity and small grain size. In contrast, the annealed sample shows a reduced peak width, indicating a reduced mosaicity and larger grain sizes.

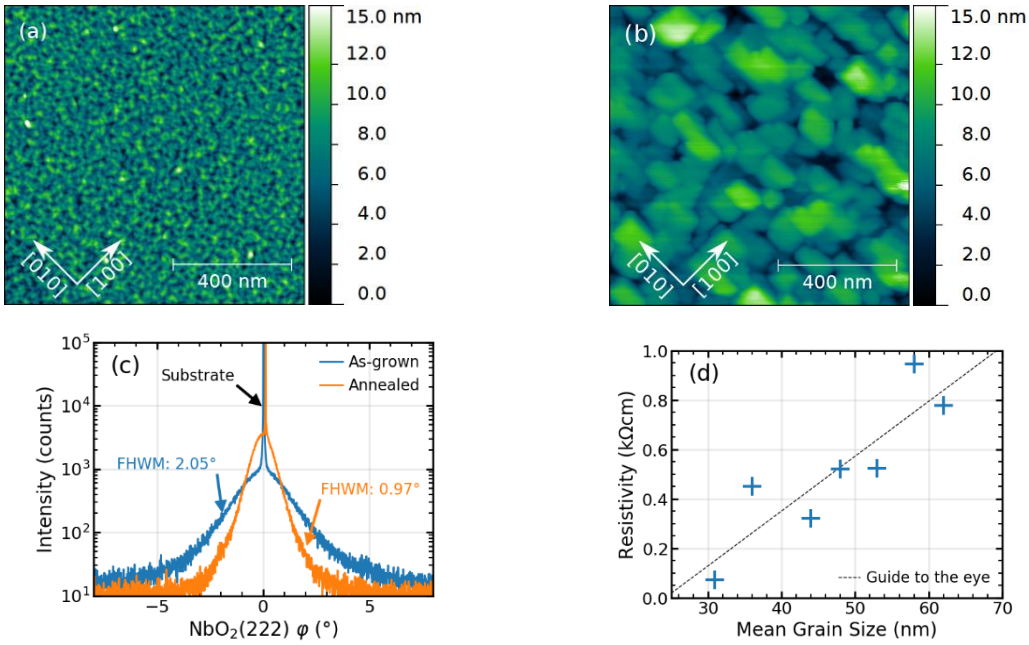

Fig 1: AFM images of the **a)** as-grown and **b)** annealed NbO_2 samples, respectively. The arrows indicate the NbO_2 orientation. **c)** Azimuthal φ-scans around the NbO_2(222) Bragg reflection **d)** Relationship of electrical conductivity and mean grain size.

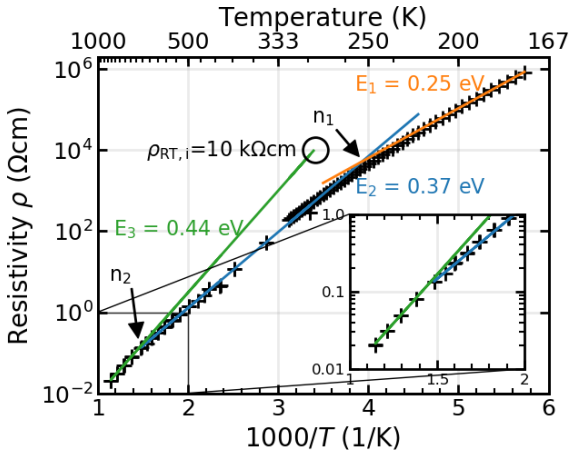

Fig 2: Electrical resistivity of an annealed NbO_2 thin film over a temperature range of 165 K to 870 K revealing three different activation energies.

The resistivity of the 100 nm as-grown sample (Fig. 1(a)) is 7 Ωcm, while the annealed layer (Fig. 1(b)) has an higher resistivity of 525 Ωcm. Several samples were grown with the post-growth annealing step, which show a spread in surface morphology and resistivity. For all annealed samples, a significant increase of the layer resistivity was found and a correlation to the average grain size was observed (Fig. 1(d)). The highest resistivity found in an annealed thin-film was 945 Ωcm, exceeding two orders of magnitude compared to as-grown thin-films. In Fig. 2, resistivity over the reciprocal temperature of an annealed sample is shown. A 1000 nm thick sample was used to raise the upper limit of the resistivity measurement to 10^6 Ωcm since at low temperatures the sample resistance rapidly exceeds values (>

10^{10} Ω) that are no longer accessible for a reliable measurement. No hysteresis effect was measured during a heating-cooling cycle, indicating a stable sample. No influence of the thickness on the resistivity was found, as the 1000 nm layer has a resistivity of 550 Ωcm at room temperature, similar to the 100 nm thick annealed sample described above. Three slopes were identified in the Arrhenius plot (Fig. 2), corresponding to three activation energies of E_1 = 0.25 eV, E_2 = 0.37 eV, and E_3 = 0.44 eV assuming $\rho \sim exp(E_i/(k_B T))$.

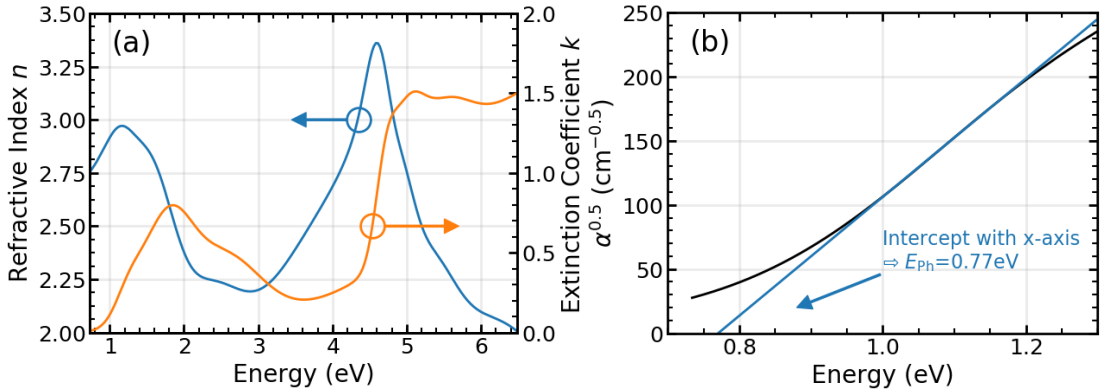

Fig 3: a) The refractive index and extinction coefficient determined by spectroscopic ellipsometry. **b)** Indirect band gap determination of annealed semiconducting NbO_2 thin film.

The refractive index *n* and extinction coefficient *k* were calculated for the dielectric function of tetragonal NbO_2(001) (Fig. 3(a)) from the SE data. The features of the spectrum are similar to the ones reported by O'Hara et al.[33] The extinction coefficient was then used to analyze the absorption edge of NbO_2 using $\alpha = 4\pi E_{Ph} k/hc$ where α is the absorption coefficient, E_{Ph} the photon energy, *c* the speed of light, and *h* the Planck constant. Using spherical parabolic band approximation at the conduction band minimum and the valence band maximum, the absorption is proportional to $\alpha \sim (E_{Ph} - E_G \pm E_{Phonon})^2$ for an indirect band gap transition.[34] The band gap transition is accompanied by a momentum conserving phonon absorption or emission. By extrapolating the linear part of the plot $\alpha^{0.5}$ over the photon energy, the intercept with the x-axis gives an energy of E_{Ph} = 0.77 eV at room-temperature.

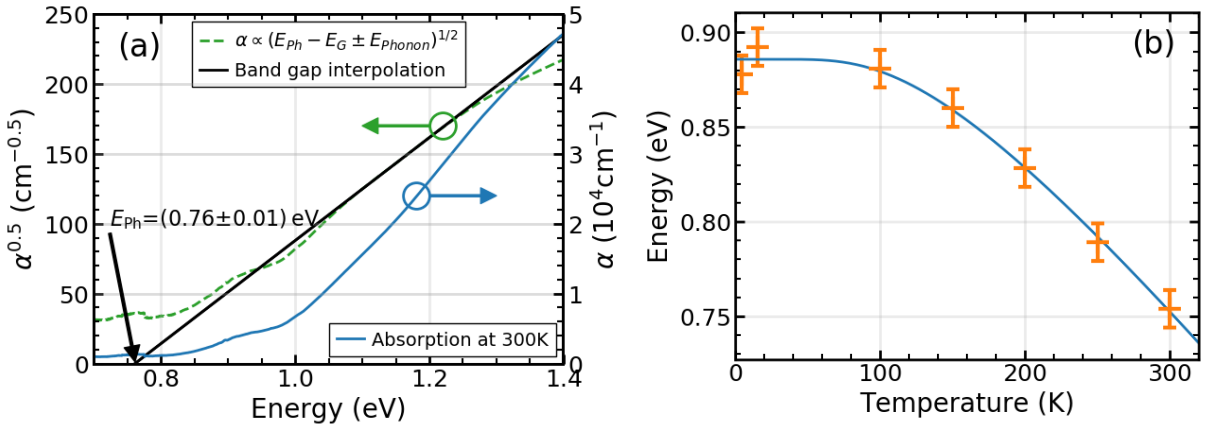

Fig 4: a) Absorption spectra and $\alpha^{0.5}$ over E plot of the NbO_2 for indirect band gap determination. **b)** Temperature-dependent measurement of the band gap for NbO_2 thin film.

Absorption spectroscopy was used as a complementary method to determine the optical band gap. The absorption spectra of NbO_2 (001) at room temperature are shown in Fig. 4(a). In order to increase the measurement sensitivity, a thin-film thickness of 1000 nm was used. The absorption coefficient could be measured up to 5×10^4 cm^{-1}. The same evaluation procedure as used for SE data was

applied to determine $E_{Ph} = E_G \pm E_{Phonon}$ from the graph shown in Fig. 4(a). An energy of (0.76 ± 0.01) eV at room temperature was determined, which is in good agreement with the SE data. The spectral dependence of the absorption coefficient measured for temperatures between 4 K and 300 K is shown in Fig. 4(b). In the low temperature region, an energy E_{Ph} = (0.89±0.02) eV is obtained which becomes temperature dependent above 80 K.

The annealing step above the phase-transition temperature has significant influence on the structural and electrical data. Janninck et al.[35] and Schäfer et al.[36] observed a change of stoichiometry to slightly oxygen-rich, single-phase $NbO_{2.006}$ after annealing the crystal above the phase-transition temperature. Oxidation with residual oxygen in the PLD chamber could explain the strong increase of the room-temperature resistivity by reducing the number of oxygen vacancies. Another explanation, taking the increased grain size into account, is a percolation like conductivity along the grain boundaries. The low-temperature semiconducting phase is formed by the dimerization of Nb-Nb d-orbitals. A break in symmetry, like it occurs at grain boundaries, could prevent the formation of the dimers and thus leading to a highly conductive phase at the grain boundaries. In fact, only a small increase of around 0.07 Å in the Nb-Nb bond could already prevent the formation of a band gap.[12] In this case, two current paths act in parallel: One along conductive (metallic) grain boundaries, the other one through the semiconducting grains. This explains the large difference of resistivity between the as-grown samples with small grains and the annealed ones with large grains and thus less conductive grain boundaries. Additionally, we have seen the correlation between grain size and resistivity (Fig 1(d)). Hence, we prefer this model to explain the conduction mechanism in our samples.

The temperature-dependent resistivity of the annealed sample (Fig. 2) exhibits thermally activated behaviour. The activation energies E_1 = 0.25 eV and E_2 = 0.37 eV are interpreted as deep levels originating from defects or impurities in the semiconducting phase inside the grains. The intercepts of the Arrhenius lines can be used to perform an order-of-magnitude estimation of the defect concentration using $n = (e\mu\rho)^{-1}$ assuming a typically low carrier mobility in oxide materials of μ = 5 cm^2/Vs. The intercepts are at 250 K and 650 K. The estimated defect concentrations are $n_1 \approx 10^{14}\,cm^{-3}$ and $n_2 \approx 10^{18}\,cm^{-3}$ for E_1 and E_2, respectively. The high-temperature resistivity decline is associated with an activation energy E_3 = 0.44 eV (Fig 2 inset). By extrapolating the high-temperature resistivity to room temperature we get a resistivity of $\rho_{RT,i}$ = 10 kΩcm, which is close to the reported intrinsic value by Janninck et al.[21] Hence, we attributed it to the thermal activation of intrinsic conductivity in the semiconductor and a band gap energy of twice the E_3 value can be estimated: E_G = 0.88 eV. This indicates, that due to the annealing of the thin-films and the resulting increase of grain size, the percolation conductivity along the grain boundaries can be neglected, as it would otherwise reduce the resistivity and the extrapolated room-temperature value of the thermally activated conductivity would not match the reported bulk resistivity value. The band gap value is higher than the optically determined value because the activation energy E_3 may contain a (small) energy portion due to the usually decreasing mobility with increasing temperature. To avoid the latter problem, Hall effect measurements for additional determination of the carrier concentration and, in turn, the mobility would have been necessary. However, reliable Hall voltage measurements were not possible most probably because of the grain structure of the films. Nevertheless, band gap values determined from ρ(T) and optical data are in reasonable agreement.

Using a model with a single harmonic oscillator, the temperature dependence of the optical band gap can be fitted with[37,38]

$$E_{Ph}(T) = E_{Ph}(0K) - S\langle\hbar\omega\rangle \coth(\langle\hbar\omega\rangle/2k_bT - 1), \qquad (3)$$

This gives an average phonon energy of $\langle\hbar\omega\rangle = (36 \pm 6)\,\mathrm{meV}$. In the energies determined in Fig. 4b, the momentum conserving phonon has to be considered in calculating the band gap value. Since at

low temperature, phonon emission is more likely than absorption, the energy has to be subtracted from the photon energy, so that we can calculate the 0 K optical band gap with $E_G = E_{Ph} - E_{Phonon} = (0.85 \pm 0.03)$ eV. The coupling constant S, a measure for the electron-phonon coupling, is 5.6 ± 0.1. The determination of the optical band gap at room temperature is more difficult, since both processes, phonon absorption, and emission can occur. We calculated an optical band gap for both, the SE and the absorption spectroscopy data to be in the range of $E_G = (0.76 \pm 0.05)$ eV. This value lies in the center of the broad range of reported optical band gap values. [10,14,23]

In summary, we have shown that a post-growth annealing step at 880 °C increases the grain size of NbO_2(001) layers epitaxially grown on MgF_2(001). Furthermore, we have shown that the resistivity correlates with the grain size and is in annealed layers up to two orders of magnitude higher than in as-grown layers. Resistivities of up to 945 Ωcm were shown, which is only one magnitude below the reported resistivity value for bulk single crystals.[21] We concluded that the conductivity of as-grown layers is dominated by a percolation conductivity along conductive grain boundaries. By reducing these conductive channels by enlarging the grains, the conductivity is now dominated by the semiconducting NbO_2 grains, which is a crucial step in the realization of resistive switching devices. The deviation of the resistivity of our layers from the values measured for single crystals could be explained by temperature-dependent resistivity measurements, which showed the presence of two defect levels in the semiconducting NbO_2. These levels contribute to the conductivity below 650 K. Above 650 K, the intrinsic conductivity becomes dominant, and an electrical band gap of 0.88 eV is estimated. This is in the range of the optical band gaps. The optical low-temperature band gap measured by absorption spectroscopy is E_G = 0.85 ± 0.03 eV. At room temperature, an optical band gap of E_G = 0.76 ± 0.05 eV was determined with ellipsometric spectroscopy as well as absorption spectroscopy. We have shown that we could increase the NbO_2 grains to an extent, that the conduction is dominated by the semiconducting phase of NbO_2, making these layers potentially suitable for resistive switching applications. However, to be able to utilize the layers in the favorable vertical device structures, a conductive substrate or a thin conductive interlayer as bottom electrode has to be used, which is part of our future work.

Supplementary Material

See supplementary material for the determination of the crystallographic orientation of the NbO_2 layer by x-ray diffraction, as well as the RHEED pattern of an annealed NbO_2 thin-film.

Acknowledgements

This work was performed in the framework of GraFOx, a Leibniz ScienceCampus. The work was partially funded by Leibniz Association under the project SAW-2017-IKZ-1, and partially by the the European Community (Europäische Fonds für Regionale Entwicklung—EFRE) under Grant No. 1.8/15.

Data Availability Statement

The data that support the findings of this study are available from the corresponding author upon reasonable request.

References

[1] G. Stefanovich, A. Pergament, and D. Stefanovich, J. Phys.: Condens. Matter **12**, 8837 (2000).
[2] P. Poddar, T. Fried, and G. Markovich, Phys. Rev. B **65**, 172405 (2002).
[3] R.M. Briggs, I.M. Pryce, and H.A. Atwater, Opt. Express **18**, 11192 (2010).
[4] E. Strelcov, Y. Lilach, and A. Kolmakov, Nano Lett. **9**, 2322 (2009).
[5] S.K. Nandi, X. Liu, D.K. Venkatachalam, and R.G. Elliman, J. Phys. D: Appl. Phys. **48**, 195105 (2015).
[6] Y. Zhou, X. Chen, C. Ko, Z. Yang, C. Mouli, and S. Ramanathan, IEEE Electron Device Lett. **34**, 220 (2013).

[7] M.D. Pickett and R. Stanley Williams, Nanotechnology **23**, 215202 (2012).
[8] R.F. Janninck and D.H. Whitmore, Journal of Physics and Chemistry of Solids **27**, 1183 (1966).
[9] K. Seta and K. Naito, The Journal of Chemical Thermodynamics **14**, 921 (1982).
[10] D. ADLER, Rev. Mod. Phys. **40**, 714 (1968).
[11] A. O'Hara and A.A. Demkov, Phys. Rev. B **91**, 094305 (2015).
[12] M.J. Wahila, G. Paez, C.N. Singh, A. Regoutz, S. Sallis, M.J. Zuba, J. Rana, M.B. Tellekamp, J.E. Boschker, T. Markurt, J.E.N. Swallow, L.A.H. Jones, T.D. Veal, W. Yang, T.-L. Lee, F. Rodolakis, J.T. Sadowski, D. Prendergast, W.-C. Lee, W.A. Doolittle, and L.F.J. Piper, Phys. Rev. Materials **3**, 074602 (2019).
[13] S. Slesazeck, H. Mähne, H. Wylezich, A. Wachowiak, J. Radhakrishnan, A. Ascoli, R. Tetzlaff, and T. Mikolajick, RSC Adv. **5**, 102318 (2015).
[14] A.B. Posadas, A. O'Hara, S. Rangan, R.A. Bartynski, and A.A. Demkov, Appl. Phys. Lett. **104**, 092901 (2014).
[15] G. Bélanger, J. Destry, G. Perluzzo, and P.M. Raccah, Can. J. Phys. **52**, 2272 (1974).
[16] A.R. Dhamdhere, T. Hadamek, A.B. Posadas, A.A. Demkov, and D.J. Smith, Journal of Applied Physics **120**, 245302 (2016).
[17] F.J. Wong, N. Hong, and S. Ramanathan, Phys. Rev. B **90**, 115135 (2014).
[18] L.E. Noskin, A.S. H, and D.G. Schlom, MRS Advances **2**, 3031 (2017).
[19] D. Music, Y.-T. Chen, P. Bliem, and R.W. Geyer, J. Phys. D: Appl. Phys. **48**, 275301 (2015).
[20] T. Joshi, Phys. Rev. Materials **3**, (2019).
[21] R.F. Janninck and D.H. Whitmore, Journal of Physics and Chemistry of Solids **27**, 1183 (1966).
[22] Y. Sakai, N. Tsuda, and T. Sakata, J. Phys. Soc. Jpn. **54**, 1514 (1985).
[23] J.C. Lee and W.W. Durand, Journal of Applied Physics **56**, 3350 (1984).
[24] E. Cha, J. Park, J. Woo, D. Lee, A. Prakash, and H. Hwang, Appl. Phys. Lett. **108**, 153502 (2016).
[25] A.K. Cheetham and C.N.R. Rao, Acta Cryst B **32**, 1579 (1976).
[26] A.A. Bolzan, C. Fong, B.J. Kennedy, and C.J. Howard, Journal of Solid State Chemistry **113**, 9 (1994).
[27] R. Pynn, J.D. Axe, and R. Thomas, Phys. Rev. B **13**, 2965 (1976).
[28] G. Vidal-Valat, J.-P. Vidal, C.M.E. Zeyen, and K. Kurki-Suonio, Acta Cryst B **35**, 1584 (1979).
[29] D. Nečas and P. Klapetek, Open Physics **10**, 181 (2011).
[30] R.M.A. Azzam and N.M. Bashara, *Ellipsometry and Polarized Light* (19870000).
[31] D. a. G. Bruggeman, Annalen der Physik **416**, 636 (1935).
[32] C.C. Katsidis and D.I. Siapkas, Appl. Opt., AO **41**, 3978 (2002).
[33] A. O'Hara, T.N. Nunley, A.B. Posadas, S. Zollner, and A.A. Demkov, Journal of Applied Physics **116**, 213705 (2014).
[34] P. YU and M. Cardona, *Fundamentals of Semiconductors: Physics and Materials Properties* (Springer Science & Business Media, 2010).
[35] R.F. Janninck and D.H. Whitmore, J. Chem. Phys. **37**, 2750 (1962).
[36] H. Schäfer, D. Bergner, and R. Gruehn, Zeitschrift für anorganische und allgemeine Chemie **365**, 31 (1969).
[37] R. Pässler, Journal of Applied Physics **89**, 6235 (2001).
[38] K.P. O'Donnell and X. Chen, Appl. Phys. Lett. **58**, 2924 (1991).